https://doi.org/10.5194/egusphere-2024-2384
Preprint. Discussion started: 28 August 2024


# Observed impacts of aerosol concentration on maritime tropical convection within constrained environments using airborne radiometer, radar, lidar, and dropsondes

Corey G. Amiot[1,#], Timothy J. Lang[2], Susan C. van den Heever[3], Richard A. Ferrare[4], Ousmane O. Sy[5], Lawrence D. Carey[1], Sundar A. Christopher[1], John R. Mecikalski[1], Sean W. Freeman[3,##], George Alexander Sokolowsky[3,###], Chris A. Hostetler[4], and Simone Tanelli[5]

[1]Department of Atmospheric and Earth Science, The University of Alabama in Huntsville, Huntsville, AL, 35899, USA
[2]NASA Marshall Space Flight Center, Huntsville, AL, 35812, USA
[3]Department of Atmospheric Science, Colorado State University, Fort Collins, CO, 80523, USA
[4]NASA Langley Research Center, Hampton, VA, 23681, USA
[5]Jet Propulsion Laboratory, California Institute of Technology, Pasadena, CA, 91109, USA

[#]Now at NASA Postdoctoral Program, NASA Marshall Space Flight Center, Huntsville, AL, 35812, USA
[##]Now at Department of Atmospheric and Earth Science, The University of Alabama in Huntsville, Huntsville, AL, 35899, USA
[###]Now at Verisk Analytics, Inc., Boston, MA, 02111, USA

*Correspondence to*: Corey G. Amiot (corey.g.amiot@nasa.gov)

**Abstract.** Aerosol modulation of atmospheric convection remains an important topic in ongoing research. A key challenge in evaluating aerosol impacts on cumulus convection is isolating their effects from environmental influences. This work investigates aerosol effects on maritime tropical convection using airborne observations from NASA's Cloud, Aerosol and Monsoon Processes Philippines Experiment (CAMP$^2$Ex). Nine environmental parameters with known physical connections to cloud and storm formation were identified from dropsonde data, and 144 dropsondes were matched with corresponding CAMP$^2$Ex flight segments ("scenes"). To constrain environmental conditions, scenes were binned based on their association with "low," "medium," or "high" values for each dropsonde-derived parameter. In each scene and environmental bin, eight radar- and radiometer-based parameters directly related to convective intensity and/or frequency were correlated with lidar-derived aerosol concentrations to examine trends in convective characteristics under different aerosol conditions. Threshold values used to stratify the environments were varied across four sensitivity tests. Convective parameters and aerosol concentrations typically became more strongly and positively correlated, with statistical significance, as environmental conditions became more favorable for convection. Particularly strong correlations between convective and aerosol metrics resulted from stratifying environments based on their 850–500-hPa temperature lapse rate (LR), 700–500-hPa LR, and K-Index. While general trends suggested that higher aerosol concentrations were correlated with stronger and/or more-frequent convection, some cases saw a "Goldilocks" zone of medium aerosol concentration favoring enhanced convection. These results indicate that medium-to-high aerosol concentrations may enhance convection, but also stress the importance of considering environmental conditions when evaluating aerosol impacts.

https://doi.org/10.5194/egusphere-2024-2384
Preprint. Discussion started: 28 August 2024


**Short summary**

Decoupling aerosol and environmental impacts on convection is challenging. Using airborne data, we correlated microwave-frequency convective metrics with aerosol concentrations in several different environments. Medium-to-high aerosol concentrations were often strongly and positively correlated with convective intensity and frequency, especially in favorable environments based on temperature lapse rates and K-Index. Storm environment is important to consider when evaluating aerosol effects.

## 1. Purpose and background

The primary purpose of this study is to explore potential impacts of aerosol concentration on maritime tropical convection during NASA's Cloud, Aerosol and Monsoon Processes Philippines Experiment (CAMP$^2$Ex) from a remote-sensing perspective within environmental contexts. This research falls under the CAMP$^2$Ex science question of "To what extent are aerosol particles responsible for modulating warm and mixed-phase precipitation in tropical environments?", while also having direct implications for impacts on deeper convection and cloud meteorology (ESPO, 2020; Reid et al., 2023). A secondary purpose of this study is to expand and demonstrate the scientific utility of geophysical retrievals from NASA's Advanced Microwave Precipitation Radiometer (AMPR; Spencer et al., 1994; Amiot et al., 2021).

A significant challenge in evaluating aerosol impacts on convection is to isolate aerosol influences from other sources of convection modulation, such as atmospheric dynamics, thermodynamics, and cloud microphysical processes (e.g., Liu et al., 2016; Grabowski 2018). Since a given convective plume will be affected by synoptic-scale (> 2000 km), mesoscale (2–2000 km), and sub-mesoscale (< 2 km) dynamics (Orlanski, 1975) and environmental conditions, it is important to understand and constrain environmental conditions associated with any convective element (herein "storm") of interest. Several environmental factors with direct physical connections to convection can be evaluated from remote-sensing and in situ observation platforms. Studies have demonstrated the utility of radiosonde data, the principles of which can be applied to dropsondes (e.g., the Advanced Vertical Atmospheric Profiling System, AVAPS; Hock and Young, 2017) to the extent offered by the dropsonde's launch altitude. Vertical velocity ($w$) at the 700-hPa level can be used to diagnose vertical motion and associated convective support (Bony et al., 2004; Liu et al., 2016). Convective Available Potential Energy (CAPE), a measure of parcel buoyancy that is used to diagnose potential updraft velocity, is defined via

$$\text{CAPE}\ \left(\text{J kg}^{-1}\right) = g\int_{z_{lfc}}^{z_{el}} \frac{(T_v - T_{v,0})}{T_{v,0}}\, dz, \quad (1)$$

where $g$ is gravitational acceleration; $T_v$ and $T_{v,0}$ are parcel and environmental virtual temperatures, respectively; $z$ is altitude; and $z_{lfc}$ and $z_{el}$ altitudes of the level of free convection and equilibrium level, respectively (Markowski and Richardson, 2010). While the shape of CAPE (Blanchard, 1998) is not examined in this study, it would be worth considering in future work given its importance to tropical convective updraft intensity.

https://doi.org/10.5194/egusphere-2024-2384
Preprint. Discussion started: 28 August 2024


The Lifting Condensation Level (LCL) altitude indicates cloud-base height and is often used in forecasting convection (Markowski and Richardson, 2010). While a surface-based parcel is expected to reach saturation faster when LCL altitude is lower (all else being equal) and thus experience warming from latent heat of condensation sooner, studies have demonstrated that higher LCL altitude is often associated with wider updrafts and stronger vertical velocities owing to entrainment of relatively dry air beneath the cloud base (Mulholland et al., 2021). K-Index is used to forecast convective potential/frequency (i.e., not intensity) and is defined as

$$\text{K-Index}(°\text{C}) = (T_{850} - T_{500}) + T_{d,850} - (T_{700} - T_{d,700}) \quad (2)$$

where $T_{850}$, $T_{700}$, and $T_{500}$ are temperatures at the 850-, 700-, and 500-hPa levels, respectively, and $T_{d,850}$ and $T_{d,700}$ are dew point temperatures at the 850- and 700-hPa levels, respectively (George, 1960). From Eq. (2), K-Index considers: 1) low-to-mid-level temperature lapse rate (hereafter simply "lapse rate", LR), 2) low-level dew point temperature ($T_d$), and 3) mid-level $T_d$ depression, with the former two (latter one) being directly (inversely) related to convective potential. In addition to 850–500-hPa, 700–500-hPa LR may serve as an excellent indicator of convective potential (e.g., Sherburn and Parker, 2014). Others (e.g., Wang et al., 2015) have used 850–700-hPa LR in forecasting convective potential due to its association with parcel vertical acceleration in the lower atmosphere. Lastly, low-level $T_d$ is important for convective intensity ("intensity" referring to peak updraft velocity) due to entrainment of relatively high-water-vapor air into an updraft's base (e.g., Lucas et al., 2000).

We utilize microwave remote-sensing signatures from radar and radiometer to evaluate convective intensity and frequency. The 30-dBZ equivalent radar reflectivity factor ($Z_H$) isoline has often been used to identify precipitation regions (e.g., Straka et al., 2000) and delineate between different "storms" or "cells" (e.g., Johnson et al., 1998; Hastings and Richardson, 2016; Amiot et al., 2019). As precipitation-sized hydrometeors form and grow, $Z_H$ increases due to hydrometeor diameter ($D$) weighting of $D^6$ associated with Rayleigh scattering, with eventual onset of non-Rayleigh resonance effects for larger values of $D$ relative to the radar wavelength (Rinehart, 2010). This is especially important to note at finer wavelengths, such as 2.2 and 0.84 cm associated with the Airborne Precipitation and cloud Radar 3rd generation (APR-3)'s Ku and Ka bands, respectively (Durden et al., 2020), the primary radar dataset used herein. A combination of Ku- and Ka-band radar can be powerful when evaluated using dual-frequency ratio (DFR):

$$\text{DFR} = Z_{Ku} - Z_{Ka}, \quad (3)$$

where $Z_{Ku}$ and $Z_{Ka}$ represent $Z_H$ at Ku- and Ka-band, respectively, on a logarithmic scale (i.e., expressed in dBZ) (e.g., Liao et al., 2008; Liao and Meneghini, 2011). In regions where $Z_{Ku}$ and $Z_{Ka}$ are both similar (e.g., near 0 dBZ for hydrometeors that are in the Rayleigh scattering regime at both frequencies), DFR will be near zero; however, departures in DFR from 0 dBZ can indicate differences in attenuation between the two frequencies and can be used to infer hydrometeor size and phase (e.g., Liao and Meneghini, 2011). As Ku-band $Z_H$ increases, the DFR in rain regions generally becomes slightly negative (i.e., -1–0) before increasing to positive values for $Z_H > 30$ dBZ; in regions of ice hydrometeors, DFR generally increases with increasing Ku-band $Z_H$, with a steeper increase occurring for lower-density ice hydrometeors (Liao and Meneghini, 2011).

https://doi.org/10.5194/egusphere-2024-2384
Preprint. Discussion started: 28 August 2024


Microwave radiometers generally retrieve higher brightness temperature ($T_b$) values at increasingly lower frequencies as precipitation hydrometeors grow in the absence of ice formation aloft (e.g., Spencer et al., 1994). This makes it possible to retrieve cloud and precipitation properties using $T_b$ combinations (e.g., Wilheit and Chang, 1980; Wentz and Spencer, 1998; Hong and Shin, 2013; Amiot et al., 2021). AMPR's cloud liquid water (CLW) retrievals often fail within precipitation regions; thus, as a cloud grows vertically, AMPR-derived CLW is expected to increase until it fails in moderate-to-heavy precipitation (Amiot et al., 2021, Amiot, 2023). However, CLW increasing around precipitation may yield useful information about the associated convective intensity; for example, precipitation is often associated with cumulus clouds at least 1.5–2 km tall (Smalley and Rapp, 2020) and CLW > 1 kg m$^{-2}$ may indicate precipitation formation within these clouds (e.g., Jiang and Zipser, 2006).

Aerosol impacts on convective storms has been a significant research topic. Increased aerosol concentration is generally associated with increased cloud condensation nuclei (CCN), with aerosol size distribution influencing cloud particle size distribution (Junge and McLaren, 1971). In shallow clouds, the second indirect effect of aerosols favors a decrease in precipitation formation and increase in cloud lifetime (Albrecht, 1989), resulting from reduced cloud droplet sizes due to increased competition for water vapor (e.g., Rosenfeld and Lensky, 1998; Sherwood, 2002). However, precipitation-sized hydrometeors that form in higher aerosol concentrations are generally larger, owing to ample cloud droplets available for collection and droplet growth (e.g., Stroud et al., 2007; Altaratz et al., 2008; Saleeby et al., 2010).

Many studies have explored aerosol warm-phase invigoration in tropical convection. Sheffield et al. (2015) demonstrated how enhanced aerosol concentrations can increase cloud water content and produce more-vigorous updrafts via latent heat of condensation. Likewise, Marinescu et al. (2021) noted a 5–15% increase in mean updraft velocity around 4–7 km AGL when CCN concentrations were relatively high. Smaller cloud droplets associated with higher aerosol concentrations may also enhance updraft/convective intensity via increased latent heat released during freezing and enhanced depositional growth above the environmental 0 °C level (e.g., van den Heever and Cotton, 2007; Rosenfeld et al., 2008). However, convective intensity increases are primarily driven by low-level condensational heating, rather than freezing above the environmental 0 °C level (Igel and van den Heever, 2021; Cotton and Walko, 2021), further indicating the importance of evaluating aerosol concentrations within/around warm-phase regions.

Despite these cloud/storm enhancements from aerosols, entrainment of relatively dry environmental air may cause rapid evaporation of smaller cloud droplets, decreasing cloud/storm structure (e.g., Liu et al., 2016). This indicates that a "Goldilocks" zone of medium aerosol concentration may favor the strongest convection (e.g., Sokolowsky et al., 2022). Additional studies demonstrated increased aerosol concentrations enhancing convection (e.g., van den Heever et al., 2006), while other research discussed considerable difficulty in separating aerosol influences from atmospheric dynamics (e.g., Grabowski, 2018), which highlights several uncertainties surrounding aerosol impacts on convection.

https://doi.org/10.5194/egusphere-2024-2384
Preprint. Discussion started: 28 August 2024


One remote-sensing instrument employed in aerosol analyses is lidar, including the High Spectral Resolution Lidar 2 (HSRL2) that deployed on NASA's P-3 aircraft during CAMP$^2$Ex (Hostetler, 2020; Reid et al., 2023; Ferrare et al., 2023). HSRL2 measures aerosol backscatter and depolarization ratio at 355, 532, and 1064 nm, with aerosol extinction and aerosol optical thickness (AOT) also measured using the HSRL2 technique at 355 and 532 nm (Hostetler, 2020). Integration for calculating AOT occurs over a vertical distance starting near the surface and ending at the top of the aerosol extinction profile, which is often around 5–6 km AGL. Lenhardt et al. (2022) demonstrated how HSRL2's extinction and backscatter coefficients, especially at 532 nm, have strong direct correlations with CCN concentrations. Additional studies (e.g., Liu et al., 2016) noted a direct correlation between lidar-based AOT and CCN concentration. Therefore, extinction, backscatter, and AOT may all be considered when examining aerosol concentration. However, the height/location of an aerosol layer, which can be obtained from extinction and/or backscatter, is important to consider when evaluating diabatic heating from radiation absorption (e.g., Chand et al., 2009; Redemann et al., 2021).

Based on these studies, the primary science question we address is: How do radiometer- and radar-based metrics of storm intensity and frequency vary with lidar-based observations of aerosol concentration when binned into similar environmental groups throughout CAMP$^2$Ex? The results of these analyses are important as they provide insight into science questions for a major NASA field campaign, have relevance to upcoming NASA missions [e.g., Atmosphere Observing System (AOS, 2022)], and contribute knowledge to long-standing questions of aerosol influences on convection. We hypothesized that radar- and radiometer-based metrics of storm intensity and frequency would all increase under greater 700-hPa $w$, CAPE, K-Index, LRs, and low-level $T_d$. Expectations for LCL altitude were more uncertain, given the greater low-level water vapor content associated with low LCL altitude, but the tendency for higher LCL altitude to favor stronger updrafts (Mulholland et al., 2021). Based on the results of Mulholland et al. (2021), we hypothesized that higher LCL altitude would correlate directly with storm intensity and frequency. Further, we hypothesized that radiometer-retrieved CLW, peak $Z_H$ and DFR, and abundance of $Z_H$ observations ≥ 30 dBZ in a given scene would all increase under higher aerosol concentrations within an environmental group. These hypotheses were based on expectations that increased aerosol concentrations would favor development of smaller and more-numerous cloud droplets, enhancing convection and CLW, while the presence of fewer but larger raindrops would increase maximum $Z_H$ and overall presence of $Z_H \geq 30$ dBZ along with greater Ka-band attenuation compared to Ku band (i.e., increased maximum DFR). While inherent difficulties, limitations, and uncertainties associated with separating aerosol and environmental influences on convection are acknowledged (e.g., Grabowski, 2018), potential trends found in the CAMP$^2$Ex dataset could provide useful information to support future work. Section 2 covers the data and methods used, with Sects. 3 and 4 highlighting environmental stratification and aerosol analyses from the microwave-frequency datasets. Section 5 presents a summary, discussion of limitations, and future work.

## 2. Data and analysis methods

All AMPR, APR-3, AVAPS, and HSRL2 data were gathered from the CAMP$^2$Ex data repository (Aknan and Chen, 2020). Due to the direct correlations between CCN concentration and lidar extinction, backscatter, and AOT, all three

https://doi.org/10.5194/egusphere-2024-2384
Preprint. Discussion started: 28 August 2024


parameters were analyzed from HSRL2's 355- and 532-nm channels that employ the HSRL2 technique, though 532-nm backscatter was of particular interest based on discussions in Lenhardt et al. (2022). The same QC processes outlined in Amiot (2023) for the AMPR, APR-3, and AVAPS data were applied for this study, including application of AMPR's multiple data quality flags and removal of the same 10 APR-3 files and 10 AVAPS dropsondes. The HSRL2 data were screened for clouds (Hostetler, 2020) to avoid potential contamination of the aerosol analyses (e.g., Liu et al., 2016). Nine environmental parameters with known physical connections to convective intensity were subjectively chosen for this study based on their ability to be fully captured by a statistically significant number of CAMP$^2$Ex dropsondes; future work would benefit from examining other environmental conditions. The nine selected parameters were: 700-hPa $w$; *modified* CAPE; LCL altitude; K-Index; 850–700-, 850–500-, and 700–500-hPa LRs; mean $T_d$ below the 925-hPa level; and mean $T_d$ below 1 km AGL, hereafter referred to by their symbols in Table 1.

Vertical ascent is a parameter included within the AVAPS dataset (Vömel et al., 2020) and is based on the fall-speed characteristics of the dropsonde (Freeman et al., 2020). The ascent value from the pressure array element nearest 700 hPa was used as $w_{700}$. Since CAPE is related to integrated buoyancy between the LFC and EL via Eq. (1), an issue arises with computing CAPE from AVAPS during CAMP$^2$Ex; since the P-3 did not fly above the EL during any science flight (SF), the dropsondes did not capture the full vertical buoyancy profile associated with traditional CAPE. As such, the term "modified CAPE" is used herein and is defined mathematically as

$$\text{CAPE}\left(\text{J kg}^{-1}\right) = g\int_{z_{lfc}}^{z_{P3}} \frac{(T_v - T_{v,0})}{T_{v,0}}\, dz, \tag{4}$$

where $z_{P3}$ is the P-3 altitude and all other terms are the same as in Eq. (1). With this definition, modified CAPE would likely be less than true CAPE within the same environment, which limits evaluation of parcel buoyancy. However, since the dropsondes were often launched when the P-3 altitude was > 4 km AGL (Vömel et al., 2020), the instability indicated by modified CAPE can be compared across the environments. Despite this, P-3 altitude would have a direct effect on modified CAPE calculated via Eq. (4), with lower altitude (e.g., around 4 km AGL) biased toward lower modified CAPE by virtue of the dropsonde capturing a lesser vertical extent of the parcel buoyancy. All CAPE values were calculated using the "mixed_layer_cape_cin" function within Python's MetPy package (May et al., 2022).

LCL altitude in each dropsonde was calculated using the "calc.lcl" function within Python's MetPy package (May et al., 2022). In contrast, the K-Index was calculated semi-manually by identifying the pressure array elements nearest the 850-, 700-, and 500-hPa levels, extracting the associated $T$ and/or $T_d$ values from these elements, and utilizing Eq. (2). In a similar manner, the temperature and altitude values from array elements nearest the 850-, 700-, and 500-hPa levels were used to calculate $LR_{850\text{-}700}$, $LR_{850\text{-}500}$, and $LR_{700\text{-}500}$ as

$$\text{LR}\left(°\text{C km}^{-1}\right) = -\frac{(T_{upper} - T_{lower})}{(z_{upper} - z_{lower})}, \tag{5}$$

where LR is lapse rate, $T_{upper}$ and $T_{lower}$ are temperatures at the higher and lower altitudes, respectively, and $z_{upper}$ and $z_{lower}$ are the higher and lower altitudes, respectively. Lastly, mean low-level $T_d$ values were calculated by finding array elements where 1) pressure was > 925 hPa, or 2) altitude was < 1 km AGL, and calculating mean $T_d$ from the associated array elements.

https://doi.org/10.5194/egusphere-2024-2384
Preprint. Discussion started: 28 August 2024


**Table 1: List of symbols used to represent the environmental, convective, and aerosol variables examined in this study, along with a brief description of each variable.**

| Symbol | Type | Description |
|---|---|---|
| $w_{700}$ | Environmental | Vertical velocity at 700-hPa level |
| CAPE | Environmental | Modified Convective Available Potential Energy |
| LCL | Environmental | Lifting Condensation Level altitude |
| K-Index | Environmental | K-Index value |
| $LR_{850-700}$ | Environmental | Temperature lapse rate between 850- and 700-hPa levels |
| $LR_{850-500}$ | Environmental | Temperature lapse rate between 850- and 500-hPa levels |
| $LR_{700-500}$ | Environmental | Temperature lapse rate between 700- and 500-hPa levels |
| $T_{d,press}$ | Environmental | Mean dew point temperature below 925-hPa level |
| $T_{d,alt}$ | Environmental | Mean dew point temperature below 1 km AGL |
| CLW | Convective | AMPR-derived columnar cloud liquid water path |
| $PCT_{10}$ | Convective | AMPR 10.7-GHz polarization-corrected temperature |
| $PCT_{19}$ | Convective | AMPR 19.35-GHz polarization-corrected temperature |
| $PCT_{37}$ | Convective | AMPR 37.1-GHz polarization-corrected temperature |
| $PCT_{85}$ | Convective | AMPR 85.5-GHz polarization-corrected temperature |
| $Z_{max,Ku}$ | Convective | APR-3 Ku-band maximum composite reflectivity |
| $Pixels_{Ku}$ | Convective | APR-3 Ku-band composite reflectivity pixels ≥ 30 dBZ |
| DFR | Convective | APR-3 Ku-/Ka-band dual-frequency ratio |
| $AOT_{355}$ | Aerosol | HSRL2 355-nm aerosol optical thickness |
| $AOT_{532}$ | Aerosol | HSRL2 532-nm aerosol optical thickness |
| $Ext_{355}$ | Aerosol | HSRL2 355-nm aerosol extinction |
| $Ext_{532}$ | Aerosol | HSRL2 532-nm aerosol extinction |
| $Bsc_{355}$ | Aerosol | HSRL2 355-nm aerosol backscatter |
| $Bsc_{532}$ | Aerosol | HSRL2 532-nm aerosol backscatter |

Once the above parameters were calculated from each dropsonde throughout CAMP$^2$Ex SFs 05–19, they were matched spatiotemporally with AMPR and APR-3 data. Since APR-3 has the highest temporal resolution of the data used herein (i.e., approximately 2 seconds per scan), the start and end times associated with each APR-3 flight-segment dataset were extracted. Each dropsonde was associated with a single APR-3 file based on which start/end times bracketed the dropsonde's launch time; for these 144 APR-3 files, the associated start and end times were used to define the "scene" times discussed below. As a result, the duration of each "scene" varied, with most scenes spanning 2–12 minutes (Fig. 1). The AMPR and HSRL2 scans nearest the start and end times of each APR-3 file were noted, and all AMPR, APR-3, and HSRL2 data were examined over the same approximate time period within each scene. Nine remote-sensing parameters related to convective intensity and/or frequency were calculated in each scene: maximum AMPR CLW; maximum AMPR polarization-corrected temperature (PCT) at 10.7, 19.35, 37.1, and 85.5 GHz; maximum APR-3 Ku-band composite $Z_H$ and DFR, and number of APR-3 Ku-band composite $Z_H$ pixels ≥ 30 dBZ, hereafter referred to by their symbols in Table 1. Maximum values were used for the former seven parameters

https://doi.org/10.5194/egusphere-2024-2384
Preprint. Discussion started: 28 August 2024


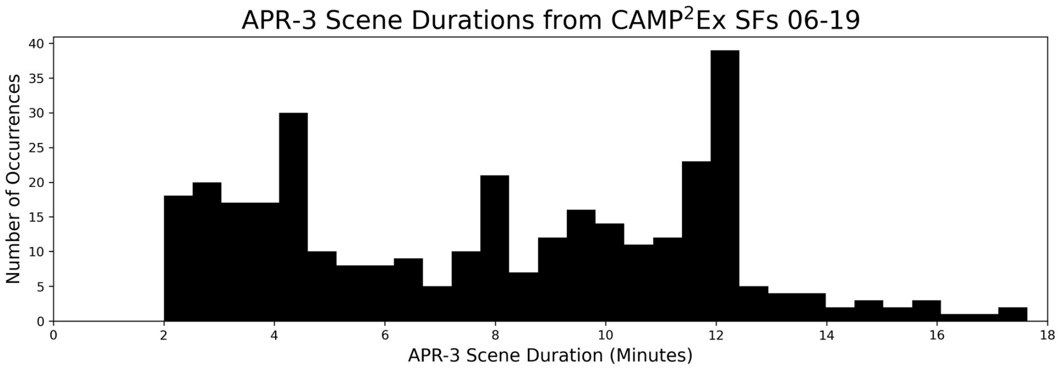


**Figure 1: Bar plot of APR-3 scene durations during CAMP²Ex SFs 06–19. SF 05 is excluded due to lack of Ku- and Ka-band APR-3 data available after applying the QC methods.**

due to their direct association with peak convective intensity. Ku-band was used for the composite $Z_H$ analyses given its reduced attenuation compared to a Ka-band signal over the same distance and atmospheric conditions (i.e., all else being equal). To calculate composite $Z_H$, the data QC described in Amiot (2023) was applied to all 25 APR-3 scan angles in each scene. Within each column of QC'd APR-3 data across SFs 05–19, the maximum $Z_H$ between the P-3 altitude and the surface was used as the composite $Z_H$. The presence of occasional residual near-surface range-/sidelobe effects at off-nadir scan angles was noted, which often manifested as very high composite $Z_H$ (i.e., > 70 dBZ). As a basic restriction, all composite $Z_H$ pixels > 70 dBZ were excluded from our analyses, but some erroneous pixels may still reside in the final dataset (e.g., isolated cases with some noisy pixels and/or near-surface range-/sidelobe effects with $Z_H$ < 70 dBZ). Once all composite $Z_H$ values were calculated, $Z_{max,Ku}$, DFR, and $Pixels_{Ku}$ were recorded in each scene. AMPR PCT values were calculated following the methods of Cecil and Chronis (2018), with their methods for 89.0-GHz data applied directly to AMPR's 85.5-GHz data. The maximum PCT in each AMPR channel was recorded along with the maximum retrieved AMPR CLW in each scene.

To begin isolating potential aerosol influences on tropical convection, two steps were employed: 1) bin the environmental scenes into different groups based on a particular AVAPS parameter and magnitude, and 2) incorporate HSRL2 data into this analysis. The nine AVAPS parameters listed in Table 1 were employed. To stratify each environment, a single AVAPS parameter was separated into "low," "medium," and "high" values, and each scene was grouped into one of these categories based on the associated dropsonde's values. Within each environmental bin, the eight convective parameters were compared against mean values of the six HSRL2 parameters (Table 1) from each scene. The main statistics examined were: Pearson correlation coefficients, the number of data points used in each comparison, and the statistical significance, primarily based on whether the p-value associated with the Pearson correlation coefficient was < 0.01 (e.g., Wilks, 2011). A few subjectively selected correlations were examined in greater detail using scatterplots, wherein it should be noted that the exact number of data points varied from plot-to-plot due to variations in missing data (e.g., dropsonde launched below the 500-hPa level for any parameters that use

https://doi.org/10.5194/egusphere-2024-2384
Preprint. Discussion started: 28 August 2024


500-hPa data). In addition, several scenes contained no unmasked APR-3 and/or AMPR data, resulting in their exclusion from the comparisons.

Lastly, the exact values used to stratify each environmental condition were varied in a sensitivity test consisting of four different sets of thresholds for each parameter (Table 2). The methods used to stratify the environmental parameters in Tests 1–4 were, respectively, as follows:

1) Create campaign-wide histograms of the AVAPS parameter and visually identify approximate values that split the dataset into three roughly equal-sized groups.
2) Use Python's "numpy.percentile" function (Harris et al., 2020) to objectively select thresholds that split each parameter's dataset into three equal-sized groups.
3) Manually select thresholds that fall between the low-medium and medium-high thresholds previously identified in Tests 1 and 2.
4) Use Python's "numpy.percentile" function to objectively select thresholds that split each parameter's dataset into three groups where the "low" and "high" categories each contain 25% of the data and the "medium" category contains 50% of the data (i.e., "medium" datasets that were approximately twice as large as the "low" and "high" datasets).

For brevity, only results from Test 2 are shown herein, but results from all four tests can be found in supplemental material. Test 2 is highlighted due to its objective stratification into roughly equal-sized groups using np.percentile.

## 3. AMPR results

This section presents the results of comparing the AMPR-based convective parameters with HSRL2 data within environmental bins established using the nine AVAPS parameters. Correlation tables are used to provide complete descriptions of the observed correlations, with more in-depth discussions and analyses performed for some subjectively selected correlations that were statistically significant and/or potentially most impactful. A brief description of the sensitivity test results for environmental stratification is provided for each parameter, and all associated correlation tables from these sensitivity tests can be found in supplemental material.

AMPR's CLW comparisons with HSRL2 in the stratified environments are summarized in Fig. 2. From Fig. 2, most Pearson correlation coefficients between the aerosol parameters and CLW were relatively low and yielded a high (i.e., > 0.05) p-value, regardless of environmental stratification, indicating generally weak correlations with limited statistical significance. This result was unexpected but, as will be elaborated upon further in this section, might have been largely due to the tendency for AMPR's CLW retrievals to fail in regions of heavy rainfall. Due to the CLW retrieval method not accounting for precipitation, regions wherein high CLW would be expected in association with heavy precipitation could easily appear as a region of failed retrieval (Amiot et al., 2021). However, clouds were screened from the HSRL2 data, so this behavior warrants further investigation. A similar trend across the HSRL2 parameters and environmental bins, albeit with different correlation values and changes in their statistical significances, was observed across the sensitivity tests performed (supplemental material).

**Table 2: List of the four sensitivity tests that were performed to stratify the nine AVAPS parameters into "low," "medium," and "high" bins. The listed values in each bracket represent the inclusive range of the "medium" bin for the respective parameter and test; that is, values less (greater) than the lower (upper) limit were classified into the "low" ("high") bin. "np" is an abbreviation for NumPy (Harris et al., 2020).**

| AVAPS parameters | Test 1: Visual histogram analysis | Test 2: np.percentile 0.33-0.33-0.33 | Test 3: Manual selection between Tests 1 and 2 | Test 4: np.percentile 0.25-0.50-0.25 |
|---|---|---|---|---|
| $T_{d,alt}$ | [21.0, 22.5] °C | [21.72, 22.4] °C | [21.35, 22.45] °C | [21.52, 22.59] °C |
| $T_{d,press}$ | [22.0, 23.0] °C | [22.62, 23.2] °C | [22.3, 23.1] °C | [22.34, 23.39] °C |
| $LR_{700\text{-}500}$ | [5.5, 6.0] °C km$^{-1}$ | [5.52, 5.9] °C km$^{-1}$ | [5.51, 5.95]°C km$^{-1}$ | [5.39, 6.01] °C km$^{-1}$ |
| $LR_{850\text{-}500}$ | [5.0, 5.5] °C km$^{-1}$ | [5.18, 5.43] °C km$^{-1}$ | [5.1, 5.47] °C km$^{-1}$ | [5.12, 5.46] °C km$^{-1}$ |
| $LR_{850\text{-}700}$ | [4.5, 5.5] °C km$^{-1}$ | [4.25, 4.98] °C km$^{-1}$ | [4.35, 5.25] °C km$^{-1}$ | [4.06, 5.11] °C km$^{-1}$ |
| K-Index | [30, 35] °C | [31.08, 35.61] °C | [30.5, 35.3] °C | [30.07, 36.59] °C |
| LCL | [400, 550] m | [404.1, 480.28] m | [402, 525] m | [369.36, 509.86] m |
| CAPE | [200, 400] J kg$^{-1}$ | [144.96, 291.65] J kg$^{-1}$ | [175, 350] J kg$^{-1}$ | [100.36, 321.48] J kg$^{-1}$ |
| $w_{700}$ | [-0.25, 0.25] m s$^{-1}$ | [-0.17, 0.06] m s$^{-1}$ | [-0.20, 0.15] m s$^{-1}$ | [-0.29, 0.12] m s$^{-1}$ |

To gain a more in-depth look at some correlations in Fig. 2, scatterplots were produced of CLW versus $Bsc_{532}$ ($AOT_{532}$) when binned by K-Index, as shown in the upper-left (upper-right) panel of Fig. 3. These correlations were selected for scatterplot analysis based on statistical significance in the CLW comparison with $AOT_{532}$ when binned by K-Index (Fig. 2), with $Bsc_{532}$ providing another aerosol comparison under similar environmental conditions. From Fig. 3, a strong positive correlation of 0.64 can be seen between CLW and $AOT_{532}$ in association with medium K-Index values, while the correlations were considerably lower for low and high K-Index values. That the medium K-Index bin stood out with statistical significance, while the low and high bins did not, is interesting, especially since a similar trend was not as prevalent in other aerosol comparisons (e.g., the scatterplot with $Bsc_{532}$ in Fig. 3) using the same environmental constraints. A majority of CLW values > 1 kg m$^{-2}$ were associated with medium or high K-Index values in both scatterplots in the upper row of Fig. 3. This CLW value of 1 kg m$^{-2}$ has been used in prior studies (e.g., Jiang and Zipser, 2006) to separate precipitating and non-precipitating clouds, which suggests that some light-to-moderate precipitation may have influenced the CLW retrievals in these cases, which coincides with an expected increased in the abundance of precipitating clouds in associated with higher K-Index values (George, 1960). The narrower spread of the medium K-Index values around this 1 kg m$^{-2}$ CLW value in the upper-right plot of Fig. 3 likely manifested as the stronger correlation coefficient. As will be referred throughout these discussions, a relatively limited sample size was present for several of the comparisons/scatterplots, and all cases examined in this study would benefit greatly from a larger sample. Despite this, the statistical significance between CLW and $AOT_{532}$ is potentially impactful, as the positive correlation matches the hypothesis that increased aerosol concentration would generally lead to higher CLW by providing more CCN and favoring the development of deeper convection due to latent heat of condensation.

Further examining the upper-right scatterplot in Fig. 3, it is interesting that several data points with CLW > 1 kg m$^{-2}$ were associated with an AOT of 0.04–0.08. Across the range of values observed in Fig. 3's upper-right plot, this would be a "medium" aerosol concentration. This is interesting and potentially impactful as it suggests the importance of the "Goldilocks" zone of medium aerosol concentration, where precipitation began to form in these clouds under

https://doi.org/10.5194/egusphere-2024-2384
Preprint. Discussion started: 28 August 2024


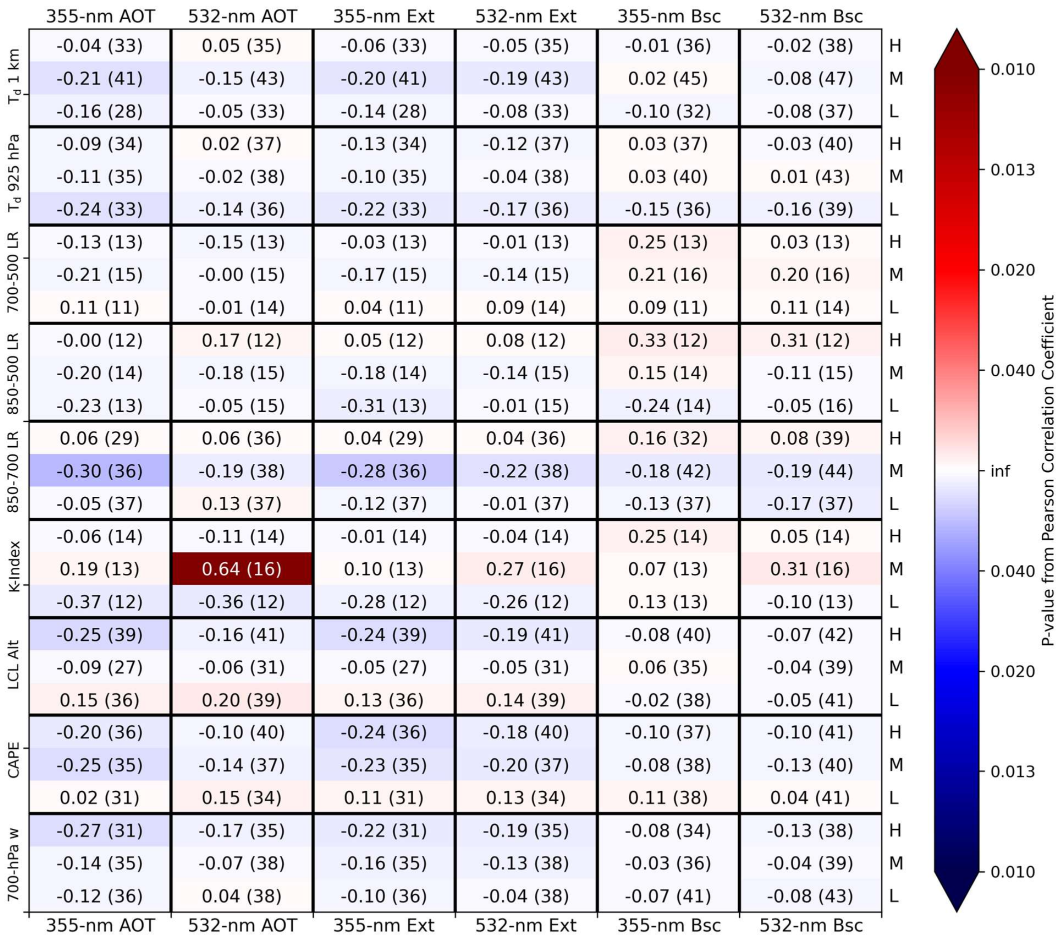


**Figure 2: Pearson correlation coefficients from comparing maximum AMPR CLW with mean HSRL2 AOT, extinction (Ext), and backscatter (Bsc) at 355 and 532 nm (top and bottom borders) within environmental bins stratified by the nine AVAPS parameters (left border) at low (L), medium (M), and high (H) magnitudes (right border) across the CAMP$^2$Ex scenes. AVAPS magnitudes were stratified using the values of Test 2 (Table 2). Within each cell, the listed value is the Pearson correlation coefficient and the parenthesized value indicates the number of data points used in the comparison. Cells with a Pearson correlation coefficient ≥ 0.70 contain bolded text. Reds (blues) represent positive (negative) Pearson correlation coefficients, and the color shading corresponds to the magnitude of the p-value according to the colorbar, with darker shades of each color associated with lower p-values (i.e., greater statistical significance). Color shading begins to increase substantially around a p-value of 0.05 and reaches a maximum for p-values around 0.01.**

the presence of medium aerosol concentration. This trend is not as pronounced in the upper-left plot of Fig. 3 and warrants further investigation, but it demonstrates the potential for medium aerosol concentrations to exert an impactful influence on the development of convection and precipitation, especially under favorable environmental conditions (i.e., medium or high K-Index values in the majority of cases observed in the upper-right plot of Fig. 3).

https://doi.org/10.5194/egusphere-2024-2384
Preprint. Discussion started: 28 August 2024


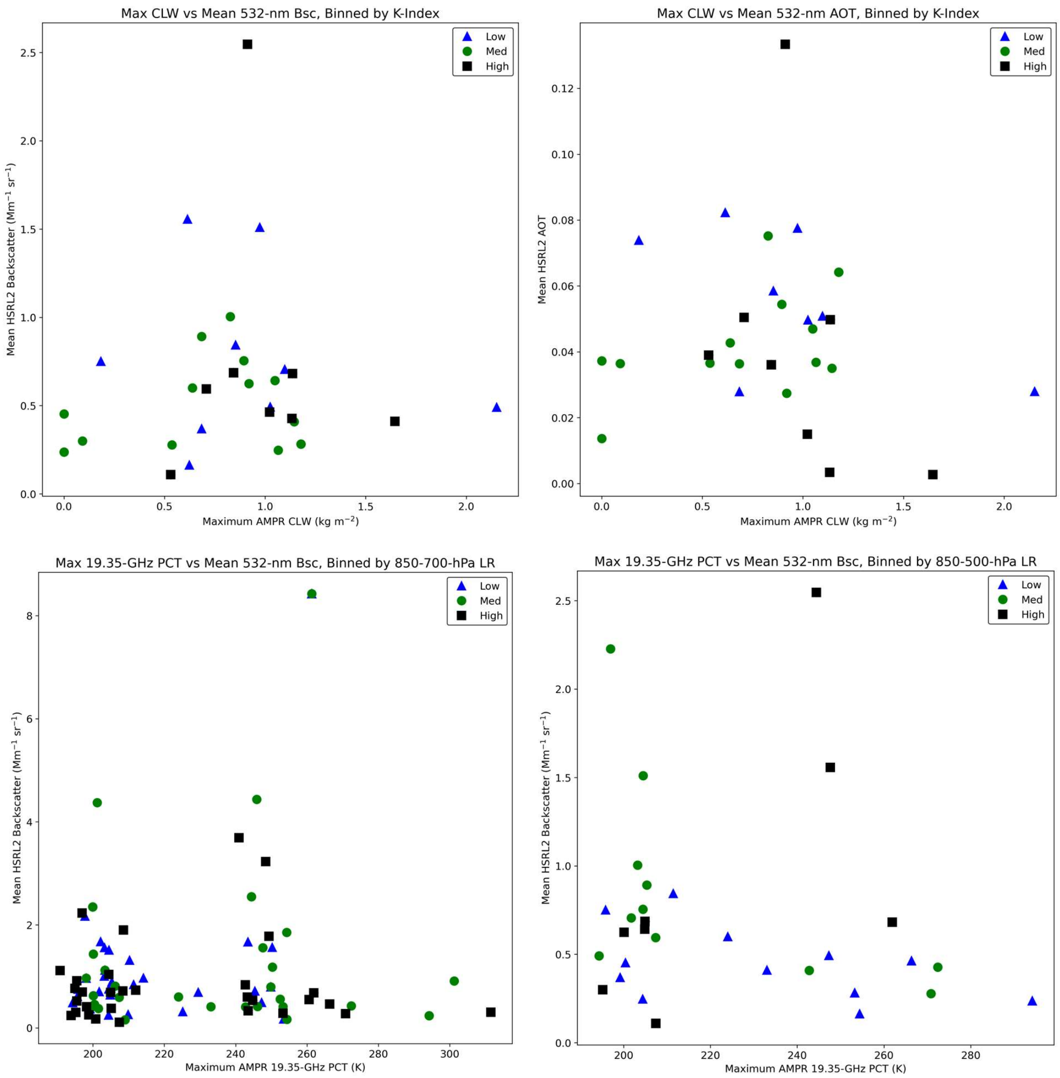


**Figure 3: Scatterplots of maximum CLW (top row) and $PCT_{19}$ (bottom row) compared with mean values of the HSRL2 parameter listed in the title and y-axis of each plot within environmental bins stratified using the AVAPS parameter listed in the title of the corresponding plot. AVAPS threshold values were from Test 2 (Table 2). In all plots, blue triangles, green circles, and black squares correspond to data points associated with low, medium, and high magnitudes, respectively, of the associated AVAPS parameter. Please note that the ranges of the x- and y-axes are not constant among the scatterplots shown.**

Despite impacts of moderate-to-heavy precipitation on CLW retrievals, AMPR $T_b$ values can be used to obtain PCTs in these regions. Correlation coefficients between AMPR's 19.35-GHz PCT and the HSRL2 parameters are shown in Fig. 4. For brevity, only $PCT_{19}$ is detailed herein given its sensitivity to clouds and precipitation, with additional PCT results presented in supplemental material. From Fig. 4, more widespread positive and statistically significant

https://doi.org/10.5194/egusphere-2024-2384
Preprint. Discussion started: 28 August 2024


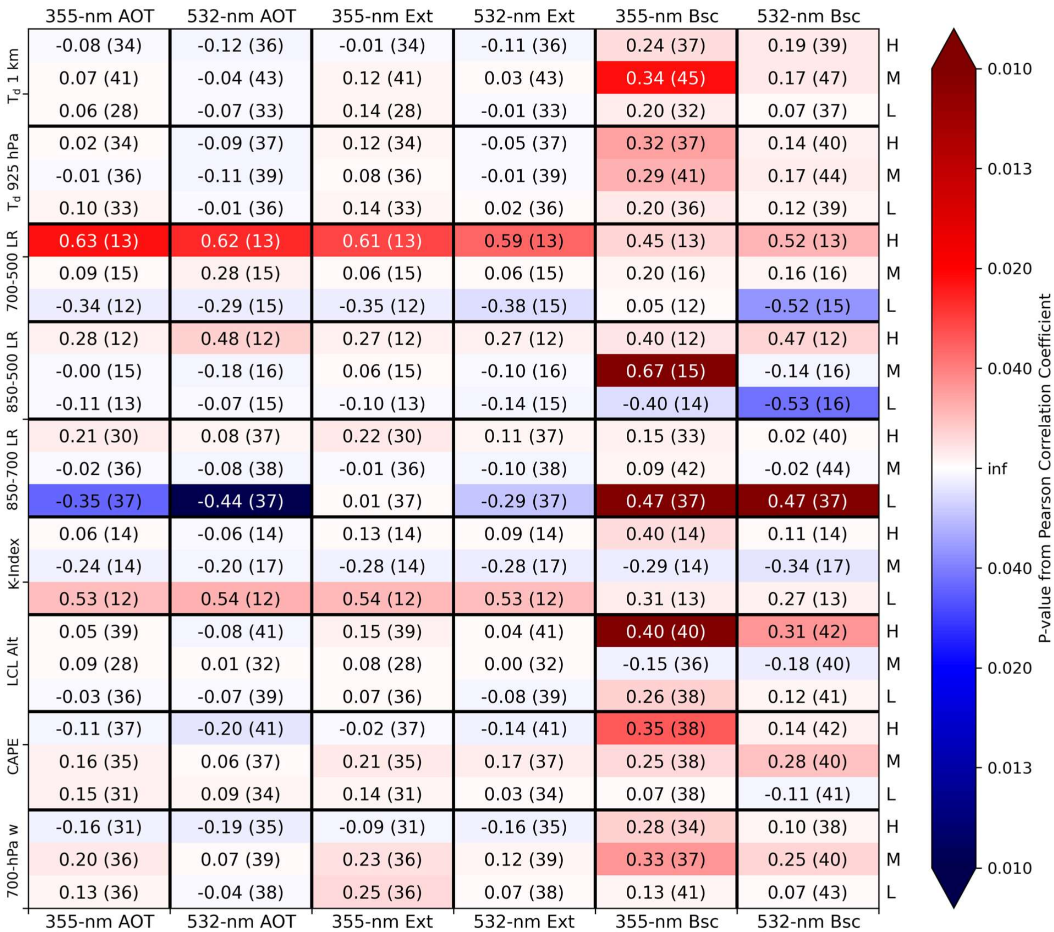


**Figure 4: As in Fig. 2 but using maximum AMPR 19.35-GHz PCT as the convective parameter.**

correlations can be seen compared to Fig. 2, indicating the potential for $PCT_{19}$ to provide insight into aerosol impacts on convection. Examining environments stratified based on LCL, $LR_{850\text{-}500}$, and $LR_{850\text{-}700}$ yielded some of the strongest and most significant correlations, especially when considering aerosol backscatter. While some negative correlations are present in Fig. 4, most of the statistically significant correlations were positive; however, it was interesting to see that the most statistically significant correlations varied between the low, medium, and high environmental bins, depending on which AVAPS variable was used for the stratification. To examine this correlation variation in greater detail, two scatterplots were produced between $PCT_{19}$ and $Bsc_{532}$. The first was based on using $LR_{850\text{-}700}$ to stratify the environments, wherein low magnitudes of LR yielded the greatest statistical significance, while the other scatterplot was based on stratification using $LR_{850\text{-}500}$, wherein the medium LR magnitudes had greatest significance.

https://doi.org/10.5194/egusphere-2024-2384
Preprint. Discussion started: 28 August 2024


From the lower-left plot in Fig. 3, the vast majority of data points with a $Bsc_{532} > 2$ $Mm^{-1}$ $sr^{-1}$ or $PCT_{19} > 240$ K were associated with a medium or high $LR_{850-700}$. The latter follows the expectation that $PCT_{19}$ would increase with increasing cloud and/or precipitation content owing to the associated increase in emissivity, since a higher $LR_{850-700}$ would indicate an increase in conditional instability and an environment that was more supportive of convection (all else being equal). The clustering of data points around a $PCT_{19}$ of 250 K is interesting, especially with the considerable variation in $Bsc_{532}$ associated with those data. Since a 250-K $PCT_{19}$ would likely be associated with at least moderate precipitation, it seems that some of the highest aerosol concentrations in these scenes correlated with the formation of precipitation. However, that the highest $PCT_{19}$ values were associated with $Bsc_{532} < 1$ $Mm^{-1}$ $sr^{-1}$ was unexpected and indicates the difficulty in separating environmental and aerosol influences on convection. A similar interesting cluster of data points around a $PCT_{19}$ of 200 K was also likely associated with the presence of clouds that were more weakly precipitating compared to those observed within the cluster around 250 K. Despite these trends, there was virtually no correlation between $PCT_{19}$ and $Bsc_{532}$ within environments binned by medium or high $LR_{850-700}$. However, there was a moderate correlation of 0.47 with statistical significance (i.e., a p-value around 0.01) between $PCT_{19}$ and $Bsc_{532}$ within environments with low $LR_{850-700}$. This was also unexpected but, as seen in Fig. 3, the increase in $PCT_{19}$ with increasing $Bsc_{532}$ within low $LR_{850-700}$ was much more gradual than within the medium and high $LR_{850-700}$ groups. That is, while there was a statistically significant correlation within the low $LR_{850-700}$ group, the highest aerosol concentrations and/or convective-parameter values were not necessarily associated with that group. Nevertheless, in environments with low $LR_{850-700}$, higher aerosol concentrations generally correlated with higher $PCT_{19}$. This makes sense physically as the low $LR_{850-700}$ group contained lapse rates up to ~4.24 °C $km^{-1}$, which are conditionally unstable.

Examining the lower-right plot in Fig. 3, which represents the same comparisons as the lower-left plot but wherein $LR_{850-500}$ was used to stratify the environments, the reduced sample size can be seen. Compared to $LR_{850-700}$, using $LR_{850-500}$ to stratify the environments resulted in two key differences: 1) the switch in correlation within low-lapse-rate environments from positive to negative, both of which were fairly statistically significant with a $p\text{-value} < 0.05$, and 2) an increase in the correlation and statistical significance of the high-lapse-rate group. Regarding the change in correlation sign for the low-lapse-rate groups, the reduced data sample in the $LR_{850-500}$ analysis resulted in most data points with $Bsc_{532} > 1$ $Mm^{-1}$ $sr^{-1}$ being excluded from the comparison. Several data points in the lower-left plot were associated with $Bsc_{532} > 1$ $Mm^{-1}$ $sr^{-1}$, and their removal yielded a trend wherein data points within the low $LR_{850-500}$ group saw a decrease in $Bsc_{532}$ as $PCT_{19}$ increased, producing the negative correlation. In contrast, the remaining high $LR_{850-500}$ data points saw a pronounced increase in $PCT_{19}$ as $Bsc_{532}$ increased, resulting in the positive correlation. The latter matches the hypothesis that higher aerosol concentrations and higher lapse rates would both favor deeper convection. However, the highest $PCT_{19}$ values in the lower-right plot of Fig. 3 were associated with $Bsc_{532} < 0.5$ $Mm^{-1}$ $sr^{-1}$, indicating that this trend is not always consistent.

Some unexpected trends in Figs. 2 and 4 should be noted, along with some caveats. First, while some patterns in Figs. 2 and 4 were constant across the different AVAPS parameters, others changed considerably depending on the parameter and threshold magnitude used to stratify the environments. In addition, while many trends were consistent

https://doi.org/10.5194/egusphere-2024-2384
Preprint. Discussion started: 28 August 2024


between HSRL2's 355- and 532-nm channels for the same AVAPS parameter, some underwent a noticeable change in Pearson correlation coefficient and/or statistical significance between the channels. Lastly, as is true for all analyses in this study, while high correlation between two parameters is interesting and potentially significant, it does not guarantee a cause-and-effect situation between the parameters. Thus, the most noteworthy trends identified in this study (e.g., Fig. 3) should be examined further to evaluate their significance and potential influences on convection.

## 4. APR-3 results

Similar analyses are presented in this section using $Z_{max,Ku}$. $Pixels_{Ku}$, and DFR as the convective parameters. All figures utilize the AVAPS thresholds from Test 2 (Table 2), with the full sensitivity-test results presented in supplemental material. To begin, Pearson correlation coefficients between $Z_{max,Ku}$ and the HSRL2 variables can be seen in Fig. 5. Several moderately and strongly positive correlations between $Z_{max,Ku}$ and HSRL2 metrics resulted from the environmental stratifications, including many with p-values < 0.01, especially when examining AOT and extinction. These trends indicate the benefits of utilizing $Z_H$ to analyze clouds and precipitation. The moderate-to-high correlations with statistical significance were also observed across many of the environmental conditions considered in the stratifications, particularly: CAPE, LCL, lapse rates, and $T_{d,press}$.

Two parameters selected for more in-depth analysis from Fig. 5 were: 1) $Ext_{532}$ binned by LCL, and 2) $Ext_{532}$ binned by $LR_{700\text{-}500}$, (Fig. 6); these were selected based on the relatively high number of statistically significant correlations found when evaluating $Ext_{532}$, with LCL and $LR_{700\text{-}500}$ offering different environmental stratifications within which to evaluate these correlations. Examining the upper-left plot of Fig. 6, all $Ext_{532}$ values > 60 $Mm^{-1}$ were associated with a medium or high LCL, which may indicate that aerosol influences on peak $Z_H$ were not as significant until the environment became more favorable for convection in general. This trend is especially pronounced for $Z_{max,Ku}$ > 50 dBZ, which may result from higher aerosol concentrations favoring the development of fewer but larger raindrops; these large raindrops would dominate $Z_H$, but this analysis also highlights the importance of considering environmental conditions. Interestingly, the correlation between $Ext_{532}$ and $Z_{max,Ku}$ was strongest and most statistically significant for low LCL values, which likely resulted from the relatively consistent low aerosol concentrations observed for the low-LCL category compared to the greater variation in aerosol concentration observed for the medium and high LCL categories (Fig. 6). As with the AMPR analyses, these scatterplot comparisons involve a relatively limited number of data points, and further investigation with a larger sample would be beneficial. It was noteworthy that several of the data points with $Z_{max,Ku}$ > 50 dBZ in the upper-left panel of Fig. 6 were associated with $Ext_{532}$ around 100–150 $Mm^{-1}$ (i.e., a "medium" aerosol concentration in this case). This also hints at the "Goldilocks" zone in aerosol concentration, where a concentration too high or low would be detrimental to convective intensity. While the overall trend is more complex and is also heavily influenced by the environmental conditions, it was interesting to see some of these medium-magnitude values stand out.

Evaluating $Z_{max,Ku}$ against $Ext_{532}$ when stratifying environments based on $LR_{700\text{-}500}$ (upper-right panel of Fig. 6), the effects of reduced sample size for any environmental parameters with a 500-hPa component can be seen, as was the

https://doi.org/10.5194/egusphere-2024-2384
Preprint. Discussion started: 28 August 2024


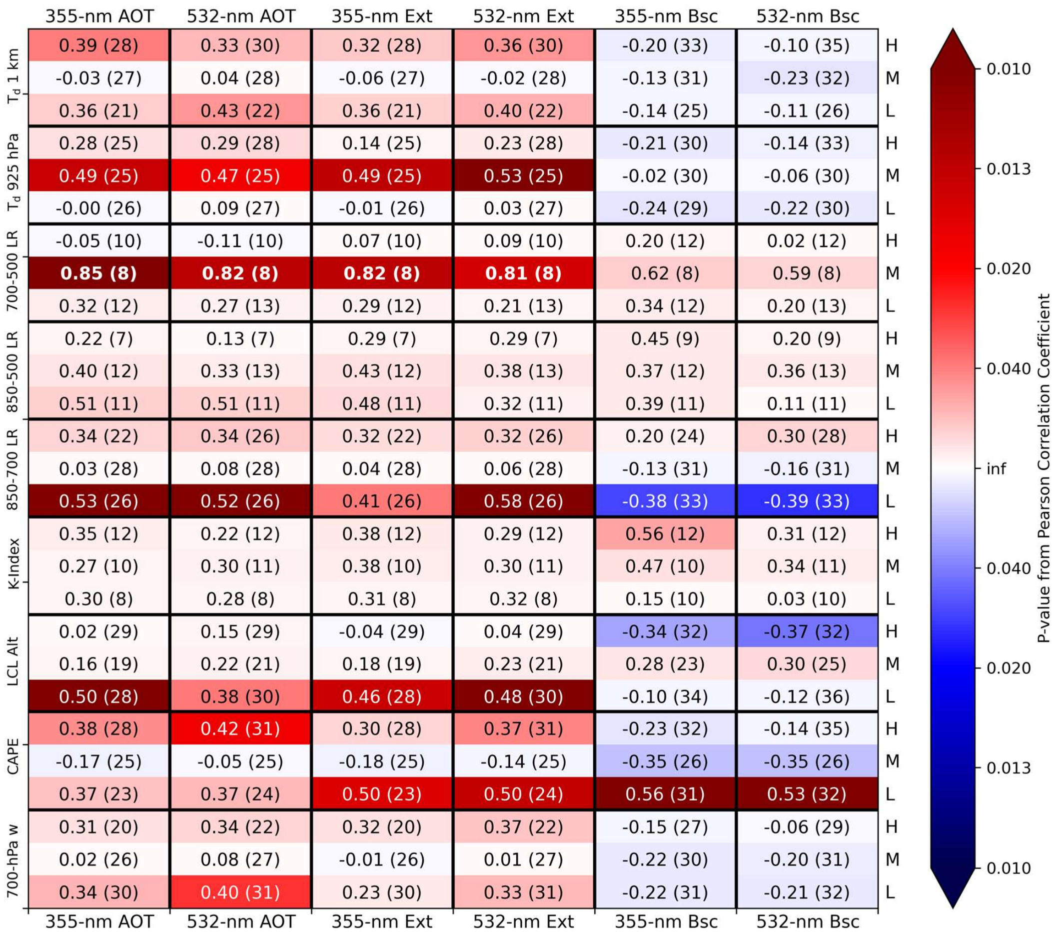


**Figure 5: As in Fig. 2 but using maximum APR-3 Ku-band composite $Z_H$ as the convective parameter.**

case with Fig. 3. The strongest and most statistically significant correlations between $Z_{max,Ku}$ and $Ext_{532}$ were found in the medium category of $LR_{700\text{-}500}$, with a trend of increasing aerosol concentration correlating with a higher $Z_{max,Ku}$. Further, the cases with $Z_{max,Ku} > 60$ dBZ were associated with a high $LR_{700\text{-}500}$, and the highest aerosol concentrations (i.e., $Ext_{532}$ around 140 $Mm^{-1}$) were associated with $Z_{max,Ku} > 50$ dBZ. These trends further suggest that many of the highest aerosol concentrations tended to be associated with relatively strong convection. The general trends in correlation and statistical significance were similar across the sensitivity tests performed (supplemental material), with some variation in the exact correlation values and p-values.

Next, the number of APR-3 Ku-band composite $Z_H$ pixels ≥ 30 dBZ (i.e., $Pixels_{Ku}$) was used as the convective parameter (Fig. 7). Several more highly positive correlations were present compared to Figs. 2, 4, and 5, likely due to $Pixels_{Ku}$ focusing on the abundance of convection rather than a peak value in a given scene. The strongest positive

https://doi.org/10.5194/egusphere-2024-2384
Preprint. Discussion started: 28 August 2024


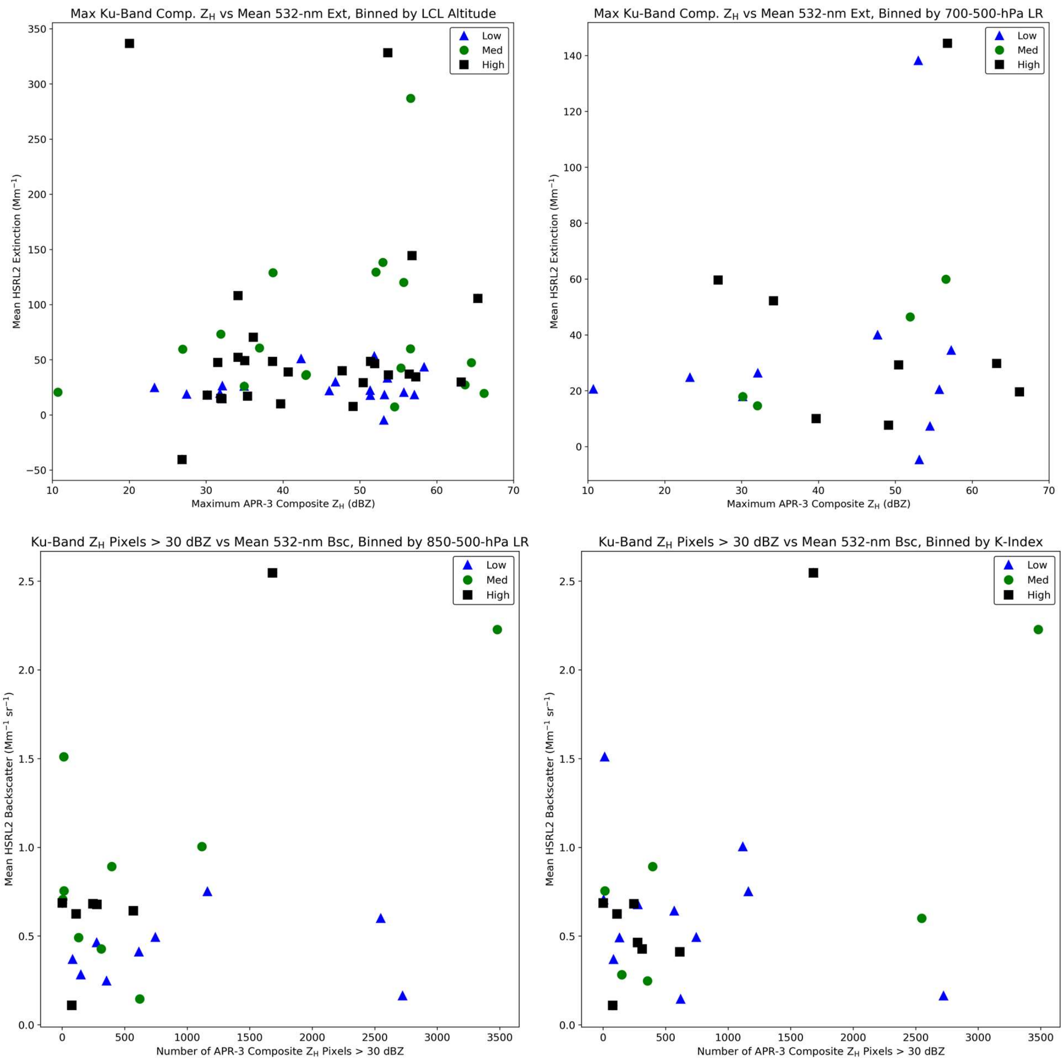


**Figure 6: As in Fig. 3, but these are scatterplots of maximum APR-3 Ku-band composite $Z_H$ (top row) and the number of APR-3 Ku-band composite $Z_H$ pixels ≥ 30 dBZ (bottom row) compared against the mean value of the HSRL2 parameter listed in the title of each plot. The AVAPS parameter used to stratify the environments is also listed in the title of each plot.**

correlations with a p-value < 0.01 were found between $Pixels_{Ku}$ and extinction at 355 and 532 nm, along with $Bsc_{532}$, especially when the environment was stratified by lapse rate or K-Index. Given the especially strong correlation between $Bsc_{532}$ and CCN concentration (Lenhardt et al., 2022) and the direct measurement of $Bsc_{532}$ by HSRL2, the decision was made to examine the strong correlations between $Pixels_{Ku}$ and $Bsc_{532}$ within environments binned by $LR_{850\text{-}500}$ and K-Index.

https://doi.org/10.5194/egusphere-2024-2384
Preprint. Discussion started: 28 August 2024


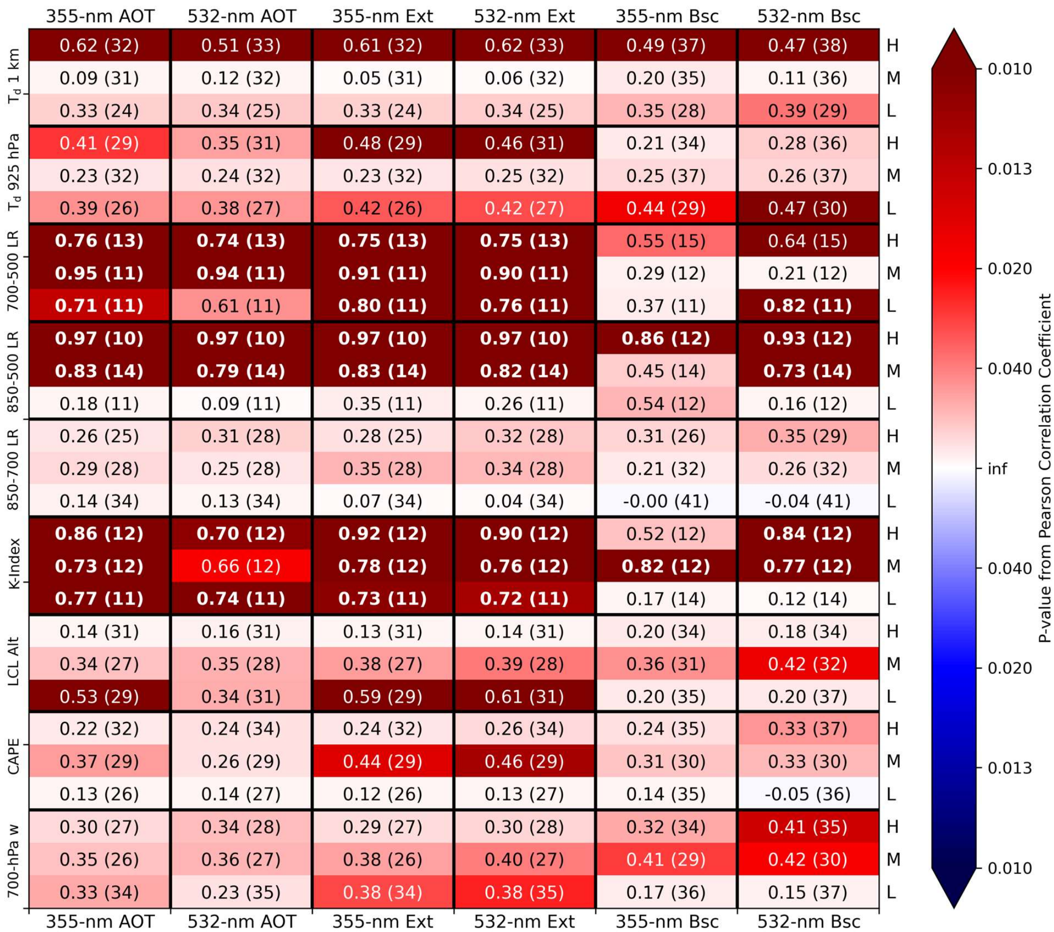


**Figure 7: As in Fig. 2 but using the number of APR-3 Ku-band composite $Z_H$ pixels ≥ 30 dBZ as the convective parameter.**

Relatively strong and statistically significant correlations observed when comparing $Pixels_{Ku}$ with $Bsc_{532}$ binned by $LR_{850\text{-}500}$ (lower-left plot of Fig. 6) may indicate the importance of considering this deeper-layer LR when evaluating aerosol influences on tropical convection (i.e., compared with the weaker correlations observed in Fig. 7 when solely considering the 850–700-hPa layer). Positive statistically significant correlations between $Pixels_{Ku}$ and $Bsc_{532}$ grew stronger as $LR_{850\text{-}500}$ increased, which matches physical expectations that higher aerosol concentration may have enhanced convection as the environment became more favorable for convection overall. Since this convective parameter is more sensitive to widespread convection rather than a peak magnitude, it seems that higher aerosol concentrations supported the development of convection in general within a given scene, regardless of whether these APR-3 pixels were part of a single large convective storm or several individual plumes. In examining the lower-left plot of Fig. 6, all cases with $Bsc_{532} > 1$ $Mm^{-1}$ $sr^{-1}$ were associated with medium or high $LR_{850\text{-}500}$ values. Further, the

https://doi.org/10.5194/egusphere-2024-2384
Preprint. Discussion started: 28 August 2024


data points (albeit only two of them) with $Bsc_{532} > 2\ Mm^{-1}\ sr^{-1}$ were associated with at least 1500 $Pixels_{Ku}$, along with a medium or high $LR_{850\text{-}500}$, which indicates that the highest aerosol concentrations in favorable environments yielded a general abundance of convection.

Binning $Pixels_{Ku}$ versus $Bsc_{532}$ comparisons by K-Index (lower-right plot in Fig. 6) also led to increasingly positive correlations as K-Index increased. This matches the hypothesis that K-Index would be associated with a relative abundance of $Pixels_{Ku}$ given the K-Index's association with convection in general (George, 1960). Correlation between convective abundance and aerosol concentration was near zero when K-Index was low but became increasingly positive as K-Index increased, especially once K-Index increased past 31.1 °C. The distribution of data points was the same across both plots in the lower row of Fig. 6, with data points binned into different environmental groups depending on whether $LR_{850\text{-}500}$ or K-Index was used for the environmental stratification. In the lower-right plot, both data points with $Bsc_{532} > 2\ Mm^{-1}\ sr^{-1}$ were associated with a medium or high K-Index value and at least 1500 $Pixels_{Ku}$, further supporting the idea that convection became more widespread as aerosol concentration increased within supportive environments. However, the two data points with 1–2 $Mm^{-1}\ sr^{-1}$ $Bsc_{532}$ were associated with low K-Index, which is reflected in their $Pixels_{Ku} < 1500$. While the differing scene times in this analysis may have had an effect, this trend further stresses the importance of considering the environment alongside aerosol concentration (i.e., many locally high aerosol concentrations were associated with a "low" K-Index) and suggests that increased aerosol concentration may not have always strongly supported convection in less-favorable environments. Most correlations in Fig. 7 were similar across the sensitivity tests (supplemental material), with environmental lapse rates and K-Index offering especially strong correlations between the convective and aerosol parameters.

Lastly, DFR was used as the convective metric (Fig. 8). As with $Z_{max,Ku}$ and unlike $Pixels_{Ku}$, DFR focuses on the intensity of a given convective storm rather than the overall abundance of convection. From Fig. 8, the most statistically significant and strongest correlations were found when binning the environments according to: CAPE, lapse rates, K-Index, or $T_{d,alt}$, typically in association with medium or high values of these environmental conditions. Due to the presence of several moderately strong correlations with p-values < 0.01, $Bsc_{355}$ was selected for deeper examination with scatterplots. Similar to the $Pixels_{Ku}$ analysis, $LR_{850\text{-}500}$ and K-Index were selected based on their relatively high correlations and statistical significance in Fig. 8, as seen in Fig. 9. A similar pattern is present in both of Fig. 9's plots, with all $Bsc_{355} > 2\ Mm^{-1}\ sr^{-1}$ associated with medium or high values of $LR_{850\text{-}500}$ and K-Index along with DFR values > 40. These high DFR values represent conditions wherein the Ka-band APR-3 data were severely attenuated, which would be expected in the strongest convection, thus matching the hypothesis that higher aerosol concentrations would coincide with stronger convection in favorable environments. However, many of the DFR values > 40 were associated with lower aerosol concentrations (i.e., $Bsc_{355} < 1.5\ Mm^{-1}\ sr^{-1}$) and a mixture of environmental conditions, with a greater number of medium and high K-Index data points found for DFR > 40 compared to the slightly greater number of low $LR_{850\text{-}500}$ data points for DFR > 40. This further indicates the importance of considering environmental conditions alongside aerosol conditions when evaluating impacts on convection. Most trends in Fig. 8 were fairly consistent among the sensitivity tests (supplemental material) apart from

https://doi.org/10.5194/egusphere-2024-2384
Preprint. Discussion started: 28 August 2024


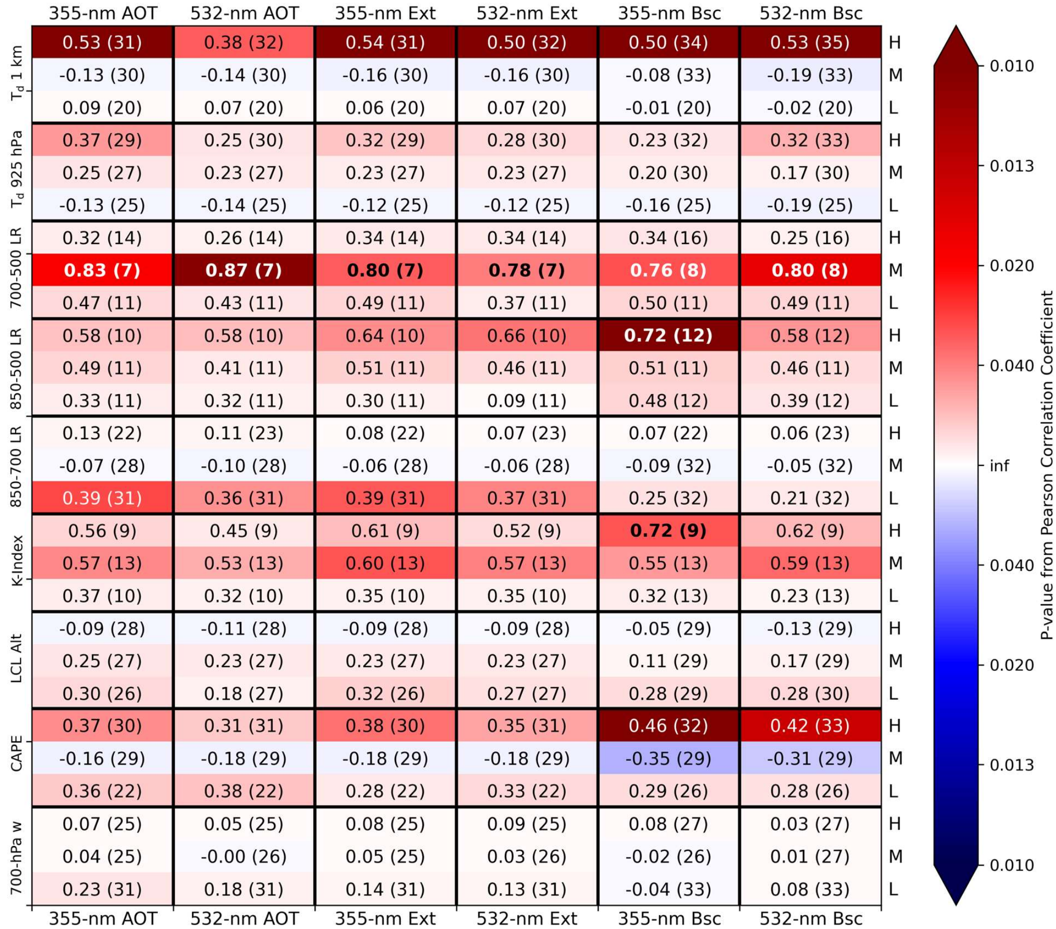


**Figure 8: As in Fig. 2 but using maximum Ku-/Ka-band DFR as the convective metric.**

some variation in the magnitude of the correlation or statistical significance. However, there were some noteworthy changes, such as the sign of the correlations among high values of $LR_{850\text{-}500}$, indicating that several of the data points may have fallen at the edges of the values used to bin the environments according to $LR_{850\text{-}500}$.

## 5. Summary, limitations, and future work

This study focused on examining potential impacts of aerosol concentration on maritime tropical convection using remote-sensing data in environmental contexts. Nine parameters from 144 AVAPS dropsondes across CAMP$^2$Ex SFs 05–19 were used to stratify the environments: 700-hPa vertical velocity; modified CAPE; LCL altitude; K-Index; 850–700-, 850–500-, and 700–500-hPa temperature lapse rates; mean $T_d$ below 1 km AGL; and mean $T_d$ below 925 hPa. Each dropsonde launch time was associated with a corresponding APR-3 scan, whose file start and end times

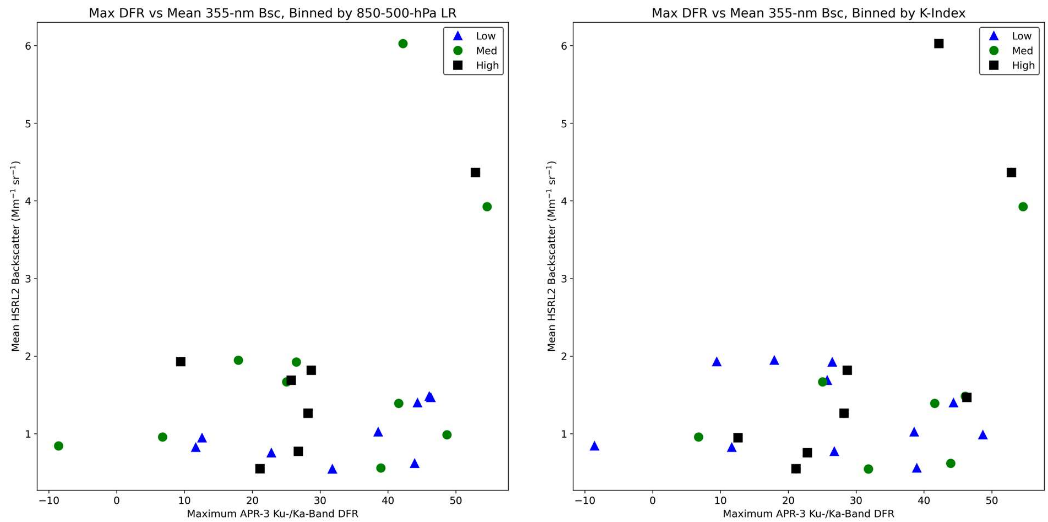


**Figure 9: As in Fig. 3, but these are scatterplots of maximum APR-3 Ku-/Ka-band DFR compared against the mean value of the HSRL2 parameter listed in the title of each plot. The AVAPS parameter used to stratify the environments is also listed in the title of each plot.**

were used to develop a "scene" for all comparisons associated with the given dropsonde. Threshold values were selected to divide scenes into "low," "medium," and "high" groups based on each AVAPS parameter, and sensitivity testing examined four different sets of threshold values used for each stratification. Eight AMPR and APR-3 metrics related to convective intensity and/or frequency were compared with HSRL2 backscatter, extinction, and AOT at 355 and 532 nm within the binned environments using Pearson correlation coefficients and their associated p-values. These convective parameters were: maximum AMPR CLW; maximum PCT at 10.7, 19.35, 37.1, and 85.5 GHz; maximum APR-3 Ku-band composite $Z_H$; number of Ku-band composite $Z_H$ pixels ≥ 30 dBZ; and Ku-/Ka-band DFR.

Several strongly positive correlations with statistical significance were observed between the convective and aerosol metrics within the environmental bins. Particularly noteworthy stratification parameters were $LR_{850-500}$ and K-Index, which yielded notable results for three of the five convective parameters detailed via scatterplots herein, and $LR_{700-500}$, which resulted in widespread strong and statistically significant correlations. Several parameters were subjectively selected for more in-depth analysis, and a full description of the correlations in each sensitivity test is provided in supplemental material. Correlations between aerosol concentrations and the convective parameters generally became more highly positive and more statistically significant, based on the associated p-value, as environmental conditions became more favorable for convection. In other words, increased aerosol concentrations appeared to enhance convection, but these effects were sometimes less significant until the environment was sufficiently supportive of convection. These results match our hypothesis that increased aerosol concentrations may contribute to stronger and/or more-widespread convection, especially in favorable environments. However, some trends hinted at a "Goldilocks" zone of aerosol concentration as demonstrated in past modeling studies, where medium aerosol

https://doi.org/10.5194/egusphere-2024-2384
Preprint. Discussion started: 28 August 2024


concentrations would be most favorable for convection compared to lower or higher values. Our results also stress the importance of considering environmental conditions alongside aerosol concentrations when evaluating impacts on convection.

These results are important as they provide observational evidence to support the idea that medium-to-high aerosol concentrations may enhance convection, which is a topic that has often been explored primarily using numerical modeling. This provides context to further our understanding of aerosol-cloud interactions and their associated impacts on the atmosphere's water and energy cycles. A key result of this study is that environmental conditions seem to be critical to the total impact aerosols may have on maritime tropical convection, where the enhancements from medium-to-high aerosol concentrations are especially prevalent in environments that are conducive for convection in general. This result does further indicate the difficulties in truly separating aerosol influences from environmental influences, but it also emphasizes the need to consider aerosol and environmental conditions together when evaluating convection. Further, the correlation tables presented in this manuscript, including those in supplemental material, provide a wide range of information that is applicable to broader applications (e.g., a future study that might explore the impacts of low-level $T_d$ or mid-level lapse rates on tropical convection).

While many results were encouraging, several limitations must be considered. Dropsondes launched when the P-3 was above 500 hPa were relatively limited, reducing the sample size for all associated environmental parameters. Other limitations in the dataset, such as the P-3 avoiding the most intense convection during a given flight and environmental modification from nearby convection, impacted the results. Further, "scene" duration varying from approximately 2–12 minutes in most cases may have affected comparisons, since lower durations were at a disadvantage when observing stronger and more-widespread convection. There was some ambiguity regarding whether an increase in $\text{Pixels}_{\text{Ku}}$ was associated with a single updraft or multiple updrafts, which have different implications for convective intensity and frequency. Lastly, while many correlations were strong and encouraging, they do not necessarily prove a cause-and-effect situation for their respective comparison. Thus, it is not possible to say with certainty that increased aerosol concentrations enhanced convection in these CAMP$^2$Ex scenes solely based on the correlations presented in this study, but rather the data suggest the possibility for aerosol enhancement of convection and further analyses would increase confidence in these results.

Given the encouraging nature of many comparisons in this study, while also considering the above limitations, future work would greatly benefit these science questions. Future efforts could look at addressing the limitations above, such as creating constant scene times across CAMP$^2$Ex, using an advanced $Z_H$ attenuation-correction method, distinguishing areas where $\text{Pixels}_{\text{Ku}}$ were adjacent or separated, and employing other datasets from the P-3 and Learjet-35 aircraft to increase reliability of the strongest correlations observed. Peak 30-dBZ $Z_H$ contour height in a storm should be considered given its direct relation to updraft magnitude (e.g., Straka et al., 2000; Amiot et al., 2019). Other remote-sensing data (e.g., satellite) may help with assessing nearby convection just outside of the P-3 observation range. Additional environmental parameters, such as wet-bulb potential temperature profiles (Williams and Renno,

1993) and the shape of CAPE, would be useful to examine. Other aerosol properties (e.g., type, composition, and hygroscopicity) and their vertical location/distribution may also be helpful to consider.

**Data availability**

The AMPR, APR-3, AVAPS, and HSRL2 data are available on the NASA Langley Research Center's Airborne Science Data for Atmospheric Composition repository at https://www-air.larc.nasa.gov/cgi-bin/ArcView/camp2ex, cited herein as Aknan and Chen (2020).

**Author contributions**

CGA performed all primary analyses and wrote the manuscript with feedback and contributions from all co-authors. TJL supervised the study, served as AMPR Principal Investigator (PI), and assisted with refining the methods and interpreting results. CGA and TJL processed the AMPR data. SCvdH and RAF served as PI for AVAPS and HSRL2, respectively. OOS processed the APR-3 data. SCvdH, RAF, OOS, LDC, SAC, and JRM assisted with refining the methods and interpreting results. SWF and GAS processed the AVAPS data. CAH processed the HSRL2 data. ST served as APR-3 PI.

**Competing interests**

The authors declare that they have no conflict of interest.

**Acknowledgements**

We are grateful to Hal Maring for financial support throughout the CAMP$^2$Ex deployment and data analyses, and to Jeff Reid for managing the CAMP$^2$Ex mission.

**Financial support**

CGA acknowledges funding from NASA Marshall Space Flight Center through Cooperative Agreement 80MSFC22M0001 with The University of Alabama in Huntsville. CGA's research was further supported by an appointment to the NASA Postdoctoral Program at NASA Marshall Space Flight Center, administered by Oak Ridge Associated Universities under contract with NASA, through contract 80HQTR21CA005.

**References**

Aknan, A., and Chen, G.: Joint data repository – CAMP2Ex, PISTON, NASA Langley Research Center, https://www-air.larc.nasa.gov/missions/camp2ex/index.html, accessed: 16 November 2020.

Albrecht, B. A.: Aerosols, cloud microphysics, and fractional cloudiness. Science, 245, 1227–1230, https://doi.org/10.1126/science.245.4923.1227, 1989.

https://doi.org/10.5194/egusphere-2024-2384
Preprint. Discussion started: 28 August 2024


Altaratz, O., Koren, I., Resin, Y., Kostinski, A., Feingold, G., Levin, Z., and Yin, Y.: Aerosols' influence on the interplay between condensation, evaporation and rain in warm cumulus cloud. Atmos. Chem. Phys., 8, 15–24, https://doi.org/10.5194/acp-8-15-2008, 2008.

Amiot, C. G.: Airborne passive microwave geophysical retrievals and applications in assessing environmental and aerosol impacts on maritime convection. Ph.D. dissertation, Dept. of Atmospheric and Earth Science, The University of Alabama in Huntsville, Huntsville, AL, 176 pp, https://louis.uah.edu/uah-dissertations/278/, 2023.

Amiot, C. G., Carey, L. D., Roeder, W. P., McNamara, T. M., and Blakeslee, R. J.: C-band dual-polarization radar signatures of wet downbursts around Cape Canaveral, Florida. Weather Forecast., 34, 103–131, https://doi.org/10.1175/WAF-D-18-0081.1, 2019.

Amiot, C. G., Biswas, S. K., Lang, T. J., and Duncan, D. I.: Dual-polarization deconvolution and geophysical retrievals from the Advanced Microwave Precipitation Radiometer during OLYMPEX/RADEX. J. Atmos. Ocean. Tech., 38, 607–628, https://doi.org/10.1175/JTECH-D-19-0218.1, 2021.

Atmosphere Observing System (AOS): Atmosphere Observing System, National Aeronautics and Space Administration, https://aos.gsfc.nasa.gov/, accessed: 16 March 2022.

Bhargava, K., Kalnay, E., Carton, J. A., and Yang, F.: Estimation of systematic errors in the GFS using analysis increments. J. Geophys. Res.-Atmos., 123, 1626–1637, https://doi.org/10.1002/2017JD027423, 2018.

Blanchard, D. O.: Assessing the vertical distribution of convective available potential energy. Weather Forecast., 13, 870–877, https://doi.org/10.1175/1520-0434(1998)013<0870:ATVDOC>2.0.CO;2, 1998.

Bony, S., Dufresne, J. L., Le Treut, H., Morcrette, J. J., and Senior, C.: On dynamic and thermodynamic components of cloud changes. *Clim. Dynam.*, **22**, 71–86, https://doi.org/10.1007/s00382-003-0369-6, 2004.

Burton, S. P., and Coauthors: Calibration of a high spectral resolution lidar using a Michelson interferometer with data examples from ORACLES. Appl. Optics, 57, 6061–6075, https://doi.org/10.1364/AO.57.006061, 2018.

Cecil, D. J., and Chronis, T.: Polarization-corrected temperatures for 10-, 19-, 37-, and 89-GHz passive microwave frequencies. J. Appl. Meteorol. Clim., 57, 2249–2265, https://doi.org/10.1175/JAMC-D-18-0022.1, 2018.

Chand, D., Wood, R., Anderson, T. L., Satheesh, S. K., and Carlson, R. J.: Satellite-derived direct radiative effect of aerosols dependent on cloud cover. Nat. Geosci., 2, 181–184, https://doi.org/10.1038/ngeo437, 2009.

Cotton, W. R., and Walko, R.: Examination of aerosol-induced convective invigoration using idealized simulations. J. Atmos. Sci., 78, 287–298, https://doi.org/10.1175/JAS-D-20-0023.1, 2021.

Durden, S., Tanelli, S., and Sy, O. O.: Product handbook for the Airborne Precipitation Radar Third Generation (APR3, all products): CAMP2Ex version 2, NASA Langley Research Center, 15 pp, https://www-air.larc.nasa.gov/cgi-bin/ArcView/camp2ex, 2020.

Earth Science Project Office (ESPO): CAMP2Ex, NASA Ames Research Center, https://espo.nasa.gov/camp2ex/content/CAMP2Ex, accessed: 25 April 2020.

Ferrare, R., and Coauthors: Airborne HSRL-2 measurements of elevated aerosol depolarization associated with non-spherical sea salt. Front. Remote Sens., 4:1143944, https://doi.org/10.3389/frsen.2023.1143944, 2023.

Freeman, S., Sokolowsky, G. A., and van den Heever, S. C.: CAMP2Ex AVAPS readme/quick start guide, NASA Langley Research Center, 6 pp, https://www-air.larc.nasa.gov/cgi-bin/ArcView/camp2ex, 2020.

Fritz, J., and Chandrasekar, V.: Simulating radar observations of precipitation at higher frequencies from lower-frequency polarimetric measurements. J. Atmos. Ocean. Tech., 29, 1435–1454, https://doi.org/10.1175/JTECH-D-11-00157.1, 2012.

Grabowski, W. W.: Can the impact of aerosols on deep convection be isolated from meteorological effects in atmospheric observations?. J. Atmos. Sci., 75, 3347–3363, https://doi.org/10.1175/JAS-D-18-0105.1, 2018.

George, J. J.: *Weather Forecasting for Aeronautics*. Academic Press, 673 pp, ISBN 9781483256450, 1960.

Harris, C. R., and Coauthors: Array programming with NumPy. Nature, 585, 357–362, https://doi.org/10.1038/s41586-020-2649-2, 2020.

Hastings, R., and Richardson, R.: Long-term morphological changes in simulated supercells following mergers with nascent supercells in directionally varying shear. Mon. Weather Rev., 144, 471–499, https://doi.org/10.1175/MWR-D-15-0193, 2016.

Hock, T., and Young, K.: GPM Ground Validation Advanced Vertical Atmospheric Profiling System (AVAPS) OLYMPEX, NASA Global Hydrology Resource Center DAAC, http://dx.doi.org/10.5067/GPMGV/OLYMPEX/AVAPS/DATA101, accessed: 13 June 2019, 2017.

Hogan, R. J., Gaussiat, N., and Illingworth, A. I.: Stratocumulus liquid water content from dual-wavelength radar. J. Atmos. Ocean. Tech., 22, 1207–1218, https://doi.org/10.1175/JTECH1768.1, 2005.

Hong, S., and Shin, I.: Wind speed retrieval based on sea surface roughness measurements from spaceborne microwave radiometers. J. Appl. Meteorol. Clim., 52, 507–516, https://doi.org/10.1175/JAMC-D-11-0209.1, 2013.

Hostetler, C. A.: CAMP2Ex HSRL-2 ReadMe, NASA Langley Research Center, 1 pp, https://www-air.larc.nasa.gov/cgi-bin/ArcView/camp2ex, 2020.

Igel, A. L., and van den Heever, S. C.: Invigoration or enervation of convective clouds by aerosols? Geophys. Res. Lett., 48, e2021GL093804, https://doi.org/10.1029/2021GL093804, 2021.

Jiang, H., and Zipser, E. J.: Retrieval of hydrometeor profiles in tropical cyclones and convection from combined radar and radiometer observations. J. Appl. Meteorol. Clim., 45, 1096–1115, https://doi.org/10.1175/JAM2386.1, 2006.

Johnson, J. T., MacKeen, P. L., Witt, A., Mitchell, E. D., Stumpf, G. J., Eilts, M. D., and Thomas, K. W.: The Storm Cell Identification and Tracking Algorithm: An enhanced WSR-88D algorithm. Weather Forecast., 13, 263–276, https://doi.org/10.1175/1520-0434(1998)013<0263:TSCIAT>2.0.CO;2, 1998.

Junge, C., and McLaren, E.: Relationship of cloud nuclei spectra to aerosol size distribution and composition. J. Atmos. Sci., 28, 382–390, https://doi.org/10.1175/1520-0469(1971)028<0382:ROCNST>2.0.CO;2, 1971.

Lang, T., Amiot, C., and Biswas, S.: AMPR CAMP2Ex, calibrated & quality-controlled flight dataset, level 2B, revision 1, NASA Langley Research Center, 16 pp, https://www-air.larc.nasa.gov/cgi-bin/ArcView/camp2ex, 2021.

Lenhardt, E. D., and Coauthors: Use of lidar aerosol extinction and backscatter coefficients to estimate cloud condensation nuclei (CCN) concentrations in the southeast Atlantic. Atmos. Meas. Tech. [preprint], https://doi.org/10.5194/amt-2022-262, 2022.

https://doi.org/10.5194/egusphere-2024-2384
Preprint. Discussion started: 28 August 2024


Liao, L., and Meneghini, R.: A study on the feasibility of dual-wavelength radar for identification of hydrometeor phases. J. Appl. Meteorol. Clim., 50, 449–456, https://doi.org/10.1175/2010JAMC2499.1, 2011.

Liao, L., Meneghini, R., Tian, L., and Heymsfield, G. M.: Retrieval of snow and rain from combined X- and W-band airborne radar measurements. IEEE T. Geosci. Remote, 46, 1514–1524, https://doi.org/10.1109/TGRS.2008.916079, 2008.

Liu, J., Li, Z., and Cribb, M.: Response of marine boundary layer cloud properties to aerosol perturbations associated with meteorological conditions from the 19-month AMF-Azores campaign. J. Atmos. Sci., 73, 4253–4268, https://doi.org/10.1175/JAS-D-15-0364.1, 2016.

Lucas, C., Zipser, E. J., and Ferrier, B. S.: Sensitivity of tropical west Pacific oceanic squall lines to tropospheric wind and moisture profiles. J. Atmos. Sci., 57, 2351–2373, https://doi.org/10.1175/1520-0469(2000)057<2351:SOTWPO>2.0.CO;2, 2000.

Marinescu, P. J., and Coauthors: Impacts of varying concentrations of cloud condensation nuclei on deep convective cloud updrafts – A multimodel assessment. J. Atmos. Sci., 78, 1147–1172, https://doi.org/10.1175/JAS-D-20-0200.1, 2021.

Markowski, P., and Richardson, Y.: *Mesoscale Meteorology in Midlatitudes.* Wiley-Blackwell, 407 pp, ISBN 9781119966678, 2010.

May, R. M., and Coauthors: MetPy: A meteorological Python library for data analysis and visualization. B. Am. Meteorol. Soc., 103, E2273–E2284, https://doi.org/10.1175/BAMS-D-21-0125.1, 2022.

Mulholland, J. P., Peters, J. M., and Morrison, H.: How does LCL height influence deep convective updraft width?. Geophys. Res. Lett., 48, e2021GL093316, https://doi.org/10.1029/2021GL093316, 2021.

Orlanski, I.: A rational subdivision of scales for atmospheric processes. B. Am. Meteorol. Soc., 56, 527–530, https://doi.org/10.1175/1520-0477-56.5.527, 1975.

Redemann, J., and Coauthors: An overview of the ORACLES (ObseRvations of Aerosols above CLouds and their intEractionS) project: Aerosol-cloud-radiation interactions in the southeast Atlantic Basin. Atmos. Chem. Phys., 21, 1507 – 1563, https://doi.org/10.5194/acp-21-1507-2021, 2021.

Reid, J. S., and Coauthors: The coupling between tropical meteorology, aerosol lifecycle, convection and the energy budget: The Cloud, Aerosol and Monsoon Processes Philippines Experiment (CAMP2Ex). B. Am. Meteorol. Soc., 106, E1179–E1205, https://doi.org/10.1175/BAMS-D-21-0285.1, 2023.

Rinehart, R. E.: *Radar for Meteorologists*. Rinehart Publications, 482 pp, ISBN 9780965800211, 2010.

Rosenfeld, D., and Lensky, I. M.: Satellite-based insight into precipitation formation processes in continental and maritime convective clouds. B. Am. Meteorol. Soc., 79, 2457–2476, https://doi.org/10.1175/1520-0477(1998)079<2457:SBIIPF>2.0.CO;2, 1998.

Rosenfeld, D., Lohmann, U., Raga, G. B., O'Dowd, C. D., Kulmala, M., Fuzzi, S., Reissell, A., and Andreae, M. O.: Flood or drought: How do aerosols affect precipitation? Science, 321, 1309–1313, https://doi.org/10.1126/science.1160606, 2008.

https://doi.org/10.5194/egusphere-2024-2384
Preprint. Discussion started: 28 August 2024


Saleeby, S. M., Berg, W., van den Heever, S., and L'Ecuyer, T.: Impact of cloud-nucleating aerosols in cloud-resolving model simulations of warm-rain precipitation in the East China Sea. J. Atmos. Sci., 67, 3916–3930, https://doi.org/10.1175/2010JAS3528.1, 2010.

Sheffield, A. M., Saleeby, S. M., and van den Heever, S. C.: Aerosol-induced mechanisms for cumulus congestus growth. J. Geophys. Res.-Atmos., 120, 8941–8952, https://doi.org/10.1002/2015JD023743, 2015.

Sherburn, K. D., and Parker, M. D.: Climatology and ingredients of significant severe convection in high-shear, low-CAPE environments. Weather Forecast., 29, 854–877, https://doi.org/10.1175/WAF-D-13-00041.1, 2014.

Sherwood, S. C.: Aerosols and ice particle size in tropical cumulonimbus. J. Climate, 15, 1051–1063, https://doi.org/10.1175/1520-0442(2002)015<1051:AAIPSI>2.0.CO;2, 2002.

Smalley, K. M., and Rapp, A. D.: The role of cloud size and environmental moisture in shallow cumulus precipitation. J. Appl. Meteorol. Clim., 59, 535–550, https://doi.org/10.1175/JAMC-D-19-0145.1, 2020.

Sokolowsky, G. A., Freeman, S. W., and van den Heever, S. C.: Sensitivities of maritime tropical trimodal convection to aerosols and boundary layer static stability. J. Atmos. Sci., 79, 2549–2570, https://doi.org/10.1175/JAS-D-21-0260.1, 2022.

Spencer, R. W., Hood, R. E., Lafontaine, F. J., Smith, E. A., Platt, R., Galliano, J., Griffin, V. L., and Lobl, E.: High-resolution imaging of rain systems with the Advanced Microwave Precipitation Radiometer. J. Atmos. Ocean. Tech., 11, 849–857, https://doi.org/10.1175/1520-0426(1994)011<0849:HRIORS>2.0.CO;2, 1994.

Straka, J. M., Zrnić, D. S., and Ryzhkov, A. V.: Bulk hydrometeor classification and quantification using polarimetric radar data: Synthesis of relations. J. Appl. Meteorol., 39, 1341–1372, doi:10.1175/1520-0450(2000)039<1341:BHCAQU>2.0.CO;2, 2000.

Stroud, C. A., and Coauthors: Cloud activating properties of aerosol observed during CELTIC. J. Atmos. Sci., 64, 441–459, https://doi.org/10.1175/JAS3843.1, 2007.

van den Heever, S. C., and Cotton, W. R.: Urban aerosol impacts on downwind convective storms. J. Appl. Meteorol. Clim., 46, 828–850, https://doi.org/10.1175/JAM2492.1, 2007.

van den Heever, S. C., Carrió, G. G., Cotton, W. R., DeMott, P. J., and Prenni, A. J.: Impacts of nucleating aerosol on Florida storms. Part I: Mesoscale simulations. J. Atmos. Sci., 63, 1752–1775, https://doi.org/10.1175/JAS3713.1, 2006.

Vömel, H., Goodstein, M., and Aredt, C.: Dropsonde data quality report: Clouds, Aerosol and Monsoon Processes-Philippines Experiment (CAMP2Ex, 2019). Version 1.0, UCAR/NCAR – Earth Observing Laboratory, https://www-air.larc.nasa.gov/cgi-bin/ArcView/camp2ex, accessed 16 November 2020.

Wang, J. K., Ford, T. W., and Quiring, S. M.: Distinguishing between unorganized and organized convection when examining land-atmosphere relationships. J. Appl. Meteorol. Clim., 54, 2229–2243, https://doi.org/10.1175/JAMC-D-15-0086.1, 2015.

Wentz, F. J., and Spencer, R. W.: SSM/I rain retrievals within a unified all-weather ocean algorithm. J. Atmos. Sci., 55, 1613–1627, https://doi.org/10.1175/1520-0469(1998)055<1613:SIRRWA>2.0.CO;2, 1998.

https://doi.org/10.5194/egusphere-2024-2384
Preprint. Discussion started: 28 August 2024


Wilheit, T. T., and Chang, A. T. C.: An algorithm for retrieval of ocean surface and atmospheric parameters from the observations of the scanning multichannel microwave radiometer. Radio Sci., 15, 525–544, https://doi.org/10.1029/RS015i003p00525, 1980.

Wilks, D. S.: *Statistical Methods in the Atmospheric Sciences*. Academic Press, 676 pp, ISBN 9780123850232, 2011.

Williams, E., and Renno, N.: An analysis of the conditional instability of the tropical atmosphere. Mon. Weather Rev., 121, 21–36, https://doi.org/10.1175/1520-0493(1993)121<0021:AAOTCI>2.0.CO;2, 1993.